

Highly crystalline Ni-doped FeP/carbon hollow nanorods as all-pH efficient and durable hydrogen evolving electrocatalysts

Lu, Xue Feng; Yu, Le; Lou, David Xiong Wen

2019

Lu, X. F., Yu, L., & Lou, D. X. W. (2019). Highly crystalline Ni-doped FeP/carbon hollow nanorods as all-pH efficient and durable hydrogen evolving electrocatalysts. *Science Advances*, 5(2), eaav6009-. doi:10.1126/sciadv.aav6009

<https://hdl.handle.net/10356/90286>

<https://doi.org/10.1126/sciadv.aav6009>

© 2019 The Authors, some rights reserved; exclusive licensee American Association for the Advancement of Science. No claim to original U.S. Government Works. Distributed under a Creative Commons Attribution NonCommercial License 4.0 (CC BY-NC).

Downloaded on 13 Mar 2024 17:29:43 SGT

ELECTROCHEMISTRY

Highly crystalline Ni-doped FeP/carbon hollow nanorods as all-pH efficient and durable hydrogen evolving electrocatalysts

Xue Feng Lu, Le Yu, Xiong Wen (David) Lou*

Herein, we report the synthesis of uniform hollow nanorods of Ni-doped FeP nanocrystals hybridized with carbon as electrocatalysts for the electrocatalytic hydrogen evolution reaction (HER). These hollow nanorods are prepared based on the etching and coordination reaction between metal-organic frameworks and phytic acid, followed by a pyrolysis process. Benefiting from the abundant active sites, the improved mass and charge transport capability, the optimized Ni-doped FeP/C hollow nanorods exhibit excellent HER activities for achieving a current density of 10 mA cm^{-2} at an overpotential of 72, 117, and 95 mV in acidic, neutral, and alkaline media, respectively, as well as superior stability. X-ray photoelectron spectroscopy and basic density functional theory calculations suggest that the improved HER activity originates from the synergistic modulation of the active components, structural and electronic properties. This protocol provides a general and friendly strategy to construct hollow phosphides for energy-related applications.

INTRODUCTION

Hydrogen generation through water splitting is considered as a green and efficient way to meet the increasing demands for renewable and clean energy sources (1, 2). As two important components of electrocatalytic water splitting, catalysts and electrolytes determine the energy transfer efficiency of hydrogen evolution reaction (HER) (3, 4). Platinum-based HER electrocatalysts are the best candidates because of their high activity and low Tafel slope, but prohibitive cost and scarcity greatly restrict their wide application (5). In the past decade, intensive research efforts have been devoted to developing nonprecious electrocatalysts, including metal alloys (5), oxides (6, 7), carbides (8), sulfides (9), nitrides (10), selenides (11), and nonmetallic electrocatalysts (12). However, very few of them show both high activity and stability for HER at all pH values. Therefore, it is of high importance to develop earth-abundant electrocatalysts for HER with high activity and stability that can function efficiently over the full pH range.

Recently, transition metal phosphides (TMPs) have attracted extensive interest in view of their low cost, nontoxicity, good chemical stability, and catalytic activity toward HER in electrolytes with a wide range of pH values (13–16). Iron phosphide (FeP) is a good conductor of heat and electricity and also has high thermal and chemical stability (17). Thus, it is better to access the active corner and edge sites on the crystallite surface, making it uniquely advantageous as an electrocatalytic material. Recently, FeP has been reported much for HER in acidic media with different morphologies, such as nanoparticles (18), nanosheets (19), microcubes (20), nanowires (21), and nanorods (22). However, few of them show comparable activity to Pt-based electrocatalysts and, even fewer show pH-universal activity and stability. One important factor hindering further improvement of catalytic activity and stability for FeP-based electrocatalysts is their low-porosity structures or the high adhesion between the surface of the catalyst and the as-formed hydrogen bubbles (23).

One popular strategy for efficient HER activity is to design and construct hollow micro/nanostructured hybrid electrocatalysts with a large number of exposed reactive active sites and reduced diffusion

length for both mass and charge transport (24, 25). Recently, metal-organic frameworks (MOFs) have been regarded as very promising platforms to obtain various micro/nanostructures, especially hollow nanostructures, because of their inherently high specific surface areas, abundant metal/organic species, and extraordinary tunability of structures and compositions (26–31). Besides, regulating the surface electronic structure and optimizing the hydrogen adsorption energy by doping of cations or anions are also important and effective strategies to improve the intrinsic activity of catalysts (13, 32). With its strong coordination ability and high phosphorus content, phytic acid with a molecular formula of $\text{C}_6\text{H}_6(\text{H}_2\text{PO}_4)_6$ is chosen recently as the phosphorus source to prepare phosphides (14). Motivated by the above considerations, we set out to design and synthesize Ni-doped FeP/C hollow nanorods using MIL-88A as the precursor and phytic acid as the etchant and phosphorus source (Fig. 1). After subsequent annealing treatment, the derived Ni-doped FeP/C material perfectly retains the structure of hollow nanorods. As a pH-universal HER electrocatalyst, the as-prepared Ni-doped FeP/C hollow nanorods show high activity and superior stability in solutions with a full pH range.

RESULTS

Materials synthesis and characterization

The morphology and structure of the as-prepared Ni-doped MIL-88A are characterized by field emission scanning electron microscopy (FESEM) and transmission electron microscopy (TEM). The FESEM and TEM images show that the Ni-doped MIL-88A samples with different Ni contents (denoted as NM-1, NM-2, and NM-3 for Ni/Fe atomic ratios of 1:3, 2:2, and 3:1 in the reactants, respectively) have similar highly uniform hexagonal rod-like solid nanostructures (Fig. 2, A to H). With the increase of doping amount, the average length of these hexagonal nanorods decreases from 3.2 to 1.6 μm , while the average width grows from 400 to 600 nm (fig. S1). X-ray powder diffraction (XRD) patterns (Fig. 2I) and Fourier transform infrared (FTIR) spectra (Fig. 2J) show that the doping process does not bring too much change in the crystal structure and composition of MIL-88A (33). With the increasing amount of nickel doping, most peaks disappear and only weak (101) and (002) crystallographic facets are reserved, implying the change of growth rates and

Copyright © 2019
The Authors, some
rights reserved;
exclusive licensee
American Association
for the Advancement
of Science. No claim to
original U.S. Government
Works. Distributed
under a Creative
Commons Attribution
NonCommercial
License 4.0 (CC BY-NC).

School of Chemical and Biomedical Engineering, Nanyang Technological University, 62 Nanyang Drive, Singapore 637459, Singapore.

*Corresponding author. Email: xwlou@ntu.edu.sg

directions (34). The results of the nitrogen sorption isotherms (Fig. 2K and fig. S2) show that the specific surface area increases with the increasing usage amount of nickel nitrate until the Ni/Fe atomic ratio in the reactant reaches 1:1. However, the specific surface area of NM-3 with a higher atomic ratio of Ni/Fe is smaller than that of NM-2. This may be due to the structural distortion of MOFs in the weakly acidic environment produced by the hydrolysis of remaining nickel ions. Besides, iron concentration and pH value also influence the particle size (33). After being treated in phytic acid solution (0.1 M) at 90°C, solid inners of the MIL-88A and Ni-doped MIL-88A samples are etched out to generate hollow nanostructures (Fig. 3). These phytic acid-treated MIL-88A (PTM) and Ni-doped MIL-88A (PTNM-1, PTNM-2, and PTNM-3 derived from NM-1, NM-2, and NM-3, respectively) hollow samples generally retain the overall rod-like appearance, but their aspect ratios become smaller after this etching and coordination reaction. When the reaction occurs at different temperatures, the nanorods could be

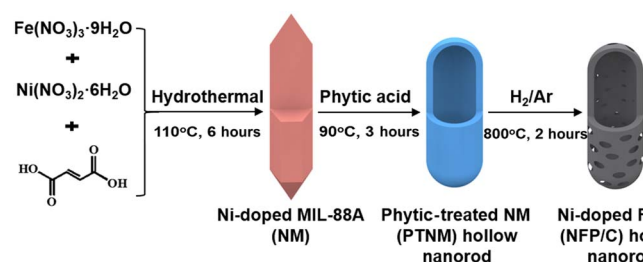


Fig. 1. Schematic illustration of the formation of Ni-doped FeP/C hollow nanorods.

transformed into well-dispersed hollow particles with core-shell/yolk-shell configurations or agglomeration of small hollow nanoparticles (fig. S3). XRD patterns indicate the phase transformation during the coordination reaction between iron ions and phytic acid (fig. S4A). The changes in FTIR peaks provide the evidence of the formation of metal-phytic compounds (fig. S4B) (35).

After a subsequent carbonization treatment, all the diffraction peaks in the XRD pattern (Fig. 4A) of the representative Ni-doped FeP/C sample derived from PTNM-3 (denoted as NFP/C-3) is consistent with an FeP standard pattern (JCPDS card no. 65-2595). No extra-neous characteristic peaks of Ni- or Fe-based materials are observed, indicating the high purity of products and the successful doping of Ni species into the lattice of FeP (20). FESEM and TEM images show that the resultant NFP/C-3 sample (Fig. 4, B and C) preserves the uniform rod-like morphology with a well-defined hollow interior. Similarly, the FeP/C sample derived from PTM and other Ni-doped FeP/C samples (NFP/C-1 derived from PTNM-1 and NFP/C-2 derived from PTNM-2) also inherit the structural features from their hollow precursors (fig. S5). A high-resolution TEM (HRTEM) image (Fig. 4D) shows that the Ni-doped FeP nanocrystals are surrounded by continuous carbon species, which is beneficial for the stability of catalysts (18). A magnified TEM image (Fig. 4E) and a corresponding line scan marked with a blue rectangle (Fig. 4F) show the lattice fringe with a spacing distance of 0.29 nm, which corresponds to the (002) planes of FeP. Elemental mapping images (Fig. 4G) show the homogenous distribution of C, P, Fe, and Ni elements in the hollow nanorod. The corresponding energy-dispersive x-ray (EDX) spectrum also confirms the existence of C, P, Fe, and Ni elements with low atomic percentage of Ni species (fig. S6).

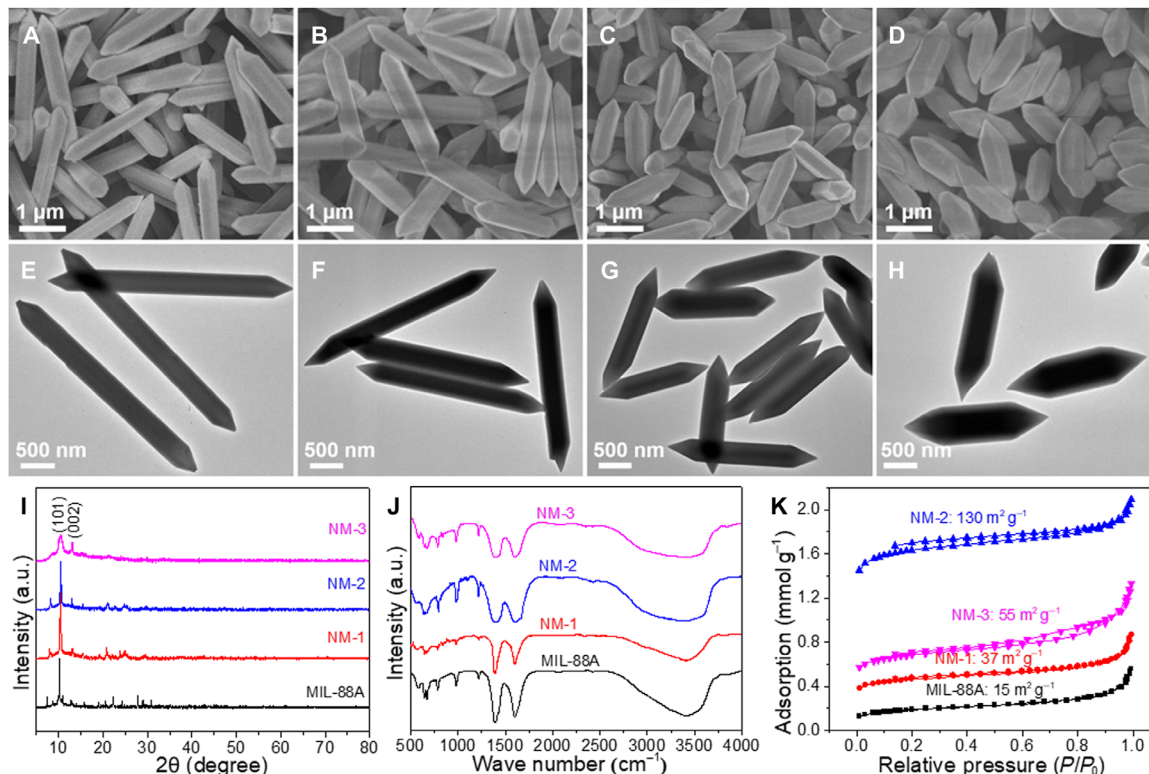


Fig. 2. The influence of doping amount on the morphology and structure of MIL-88A. (A to D) FESEM images and (E to H) TEM images of as-prepared (A and E) MIL-88A, (B and F) NM-1, (C and G) NM-2, and (D and H) NM-3. (I) XRD patterns, (J) FTIR spectra, and (K) nitrogen sorption isotherms of MIL-88A, NM-1, NM-2, and NM-3. a.u., arbitrary units.

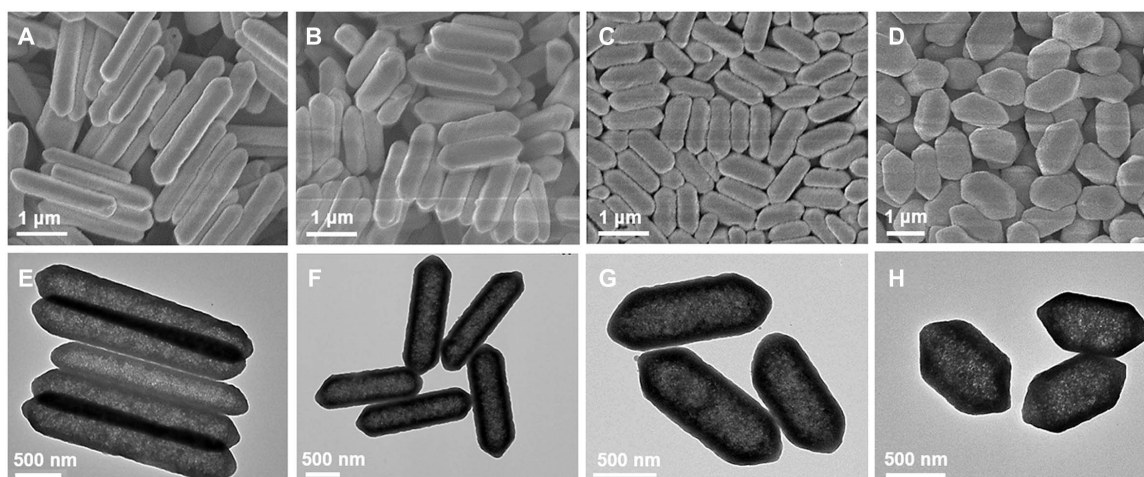


Fig. 3. Morphology and structure characterizations of MIL-88A treated with phytic acid. (A to D) FESEM images and (E to H) TEM images of (A and E) PTM, (B and F) PTNM-1, (C and G) PTNM-2, and (D and H) PTNM-3 hollow nanorods.

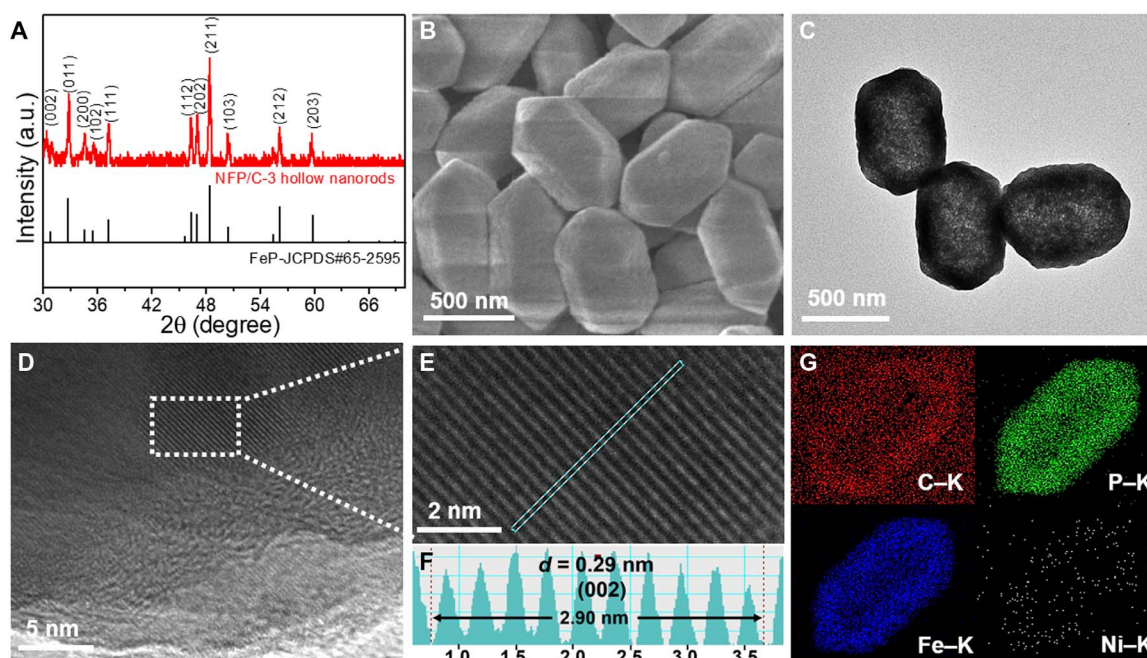


Fig. 4. Morphology and structure characterizations of NFP/C-3 hollow nanorods. (A) XRD pattern, (B) FESEM image, (C) TEM image, (D and E) HRTEM images, (F) line scan of the HRTEM image indicated by the blue rectangle in (E), and (G) elemental mapping.

The atomic ratio of Ni/Fe for NFP/C-3 from the EDX is consistent with the results of inductively coupled plasma atomic emission spectroscopy with a value of 4/235. More information about carbon species in the resultant phosphides is provided by the Raman spectra (fig. S7) (20, 36). The analogical locations and peak intensity ratio of D and G bands (located at 1335 and 1596 cm^{-1}) for FeP/C and three NFP/C samples indicate that the Ni ions should have been dominantly incorporated into the FeP lattice instead of carbon. Nitrogen adsorption/desorption isotherms (fig. S8) show that NFP/C-3 has the largest specific surface area of 72 $\text{m}^2 \text{g}^{-1}$ with an average pore size of about 3 nm. The pore size distributions of the four phosphide samples appear to be very similar, which may also suggest that nickel atoms are

doped into the lattice of FeP. The mesoporous structure facilitates to the electroactive surface, which is beneficial for enhancing HER performance (20).

Electrochemical performances

To investigate the doping effect for HER, we first compare the catalytic performances of bare FeP/C and Ni-doped FeP/C hollow nanorods in acidic medium (0.5 M H_2SO_4 solution, $\text{pH} \approx 0$). The used reference electrode is calibrated before tests (fig. S9). As shown in linear sweep voltammetry (LSV) curves (Fig. 5A), with the increase of doping amount, the overpotential required to reach the current density of 10 mA cm^{-2} becomes lower. The specific comparison of electrocatalytic

performance of the four catalysts in 0.5 M H_2SO_4 solution is listed in table S1. The overpotential at 10 mA cm^{-2} of NFP/C-3 hollow nanorods is only 72 mV, which is not only much smaller than that of the FeP/C sample (157 mV) but also comparable to those of many other transition metal-based phosphides (table S2), implying superior electrocatalytic activity. Moreover, the NFP/C-3 hollow nanorods show the smallest onset overpotential of ~ 22 mV versus reversible hydrogen electrode (RHE) (fig. S10). Considering the negligible activity contribution from a carbon fiber paper (CFP) substrate (fig. S11), we attribute the improvement in electrocatalytic performance to the doping effect. Besides, we have also prepared NFP/C-3 with low crystallinity and NFP-3 without carbon as control samples. NFP/C-3 with low crystallinity can only be obtained by annealing PTNM-3 at 800°C for a shorter period (fig. S12). All the electrochemical data including the overpotential at 10 mA cm^{-2} , Tafel slope, stability, and charge transfer resistance (R_{ct}) show the superiority of NFP/C-3 with high crystallinity (fig. S13). For comparison, a sample named NFP-3 without carbon is prepared by annealing the phytic acid-treated oxide sample derived from NM-3. Structural analyses (fig. S14) show that the structure of NFP-3 without carbon is destroyed severely. Degradations of electrocatalytic activity and stability (fig. S15) highlight the importance of carbon for structural integrity and catalytic performance.

To further study the underlying electrocatalytic mechanism for HER, the corresponding Tafel plots based on the LSV curves are presented in Fig. 5B. These linear regions of Tafel plots are fitted to the Tafel equation ($\eta = b \log j + a$, where b is the Tafel slope), yielding Tafel slopes of 127, 87, 81, and 54 mV decade^{-1} for FeP/C, NFP/C-1, NFP/C-2, and NFP/C-3 hollow nanorods, respectively. The Tafel slope of NFP/C-3 hollow nanorods indicates that HER occurs via the Volmer-Heyrovsky mechanism and the electrochemical recombination with an additional proton is the rate-limiting step (37, 38). The exchange current density (J_0) for each sample is obtained by extrapolation of the

corresponding Tafel plot (fig. S16). The J_0 of NFP/C-3 hollow nanorods is ~ 0.723 mA cm^{-2} , which outperforms that of the FeP/C sample (0.594 mA cm^{-2}) and those of many transition metal-based phosphides (table S2). The electrochemically active surface area (ECSA) of catalysts is further evaluated through electrochemical double-layer capacitance (fig. S17). Herein, NFP/C-3 hollow nanorods exhibit a capacitance of 80.2 mF cm^{-2} , which is much larger than that of FeP/C hollow nanorods (Fig. 5C), indicating more exposed electrochemically active sites. Electrochemical impedance spectroscopy (EIS) data (fig. S18) also show the reduced solution resistance (R_s) and R_{ct} for the Ni-doped samples due to the improvement in hydrophilicity and conductivity caused by the dopant (39). The results of the hydrophilic test further indicate the improvement in hydrophilicity with a smaller contact angle (fig. S19).

It is noteworthy that numerous microbial and strongly alkaline electrolysis cells need active and stable electrocatalysts in neutral and basic conditions (6). These Ni-doped FeP/C hollow nanorods show high HER activities with an onset overpotential of ~ 55 mV (fig. S20A) and a small overpotential of 117 mV at 10 mA cm^{-2} (Fig. 5D) in a neutral solution [1.0 M phosphate-buffered saline (PBS) solution, $\text{pH} \approx 7$]. Compared with the FeP/C sample, the corresponding smaller Tafel slope (inset in Fig. 5D) and higher exchange current density of the doped hollow nanorods (fig. S20B) indicate the favorable dynamic process in neutral environment. Moreover, NFP/C-3 hollow nanorods reveal high electrocatalytic performance in a strongly alkaline solution (1.0 M KOH solution, $\text{pH} \approx 14$). Once again, the doped hollow nanorods demonstrate better HER activities over the FeP/C sample with smaller overpotential and Tafel slope (Fig. 5E). In addition, these Ni-doped FeP/C hollow nanorods show enhanced properties with smaller onset overpotential and higher exchange current density (fig. S20, C and D). The activities of NFP/C-3 are also comparable to those of many reported nonprecious metal-based HER

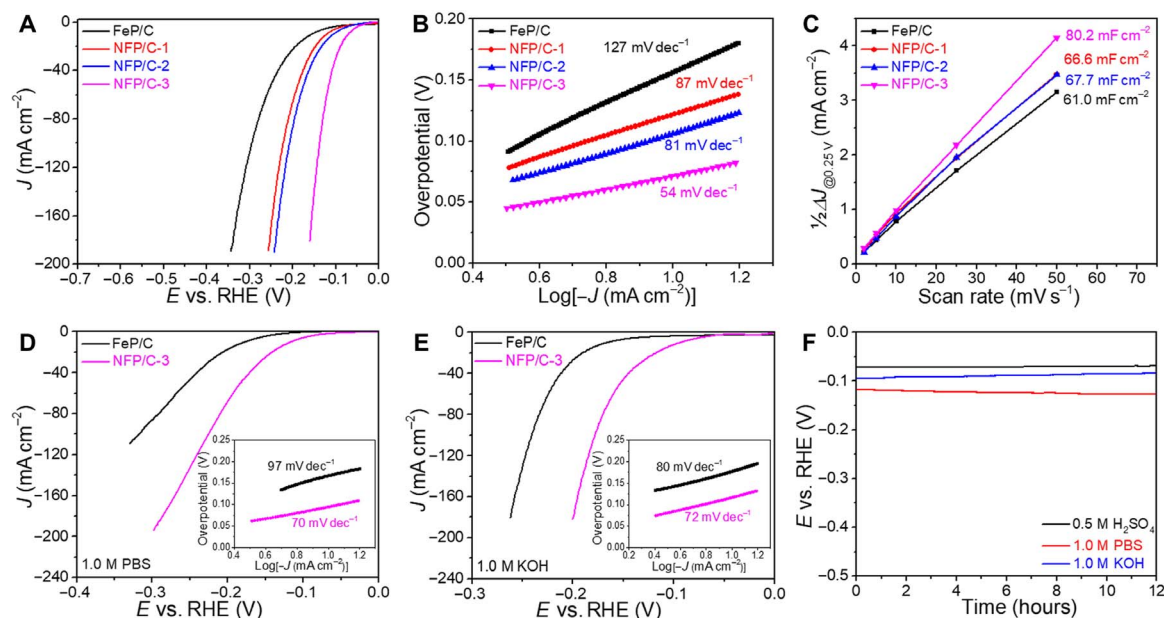


Fig. 5. Electrochemical performances of electrocatalysts measured in acidic, neutral, and alkaline solutions. (A) LSV curves, (B) corresponding Tafel slopes, and (C) the capacitive current density $\Delta j_{0.25 \text{ V}}$ as a function of scan rate in the range of 0.2 to 0.3 V versus RHE in 0.5 M H_2SO_4 of FeP/C, NFP/C-1, NFP/C-2, and NFP/C-3. LSV curves of FeP/C and NFP/C-3 in (D) 1.0 M PBS and (E) 1.0 M KOH solutions (insets: Tafel slopes). (F) Chronopotentiometry curves at a constant current density of 10 mA cm^{-2} for 12 hours of NFP/C-3 in 0.5 M H_2SO_4 , 1.0 M PBS, and 1.0 M KOH solutions.

electrocatalysts in neutral and basic conditions (tables S3). Chronopotentiometric response measurement shows that the NFP/C-3 hollow nanorods stably run over 12 hours at a current density of 10 mA cm^{-2} without obvious amplification in overpotential in acidic, neutral, and alkaline solutions (Fig. 5F). The LSV curves for NFP/C-3 hollow nanorods before and after the stability test also indicate superior stability. We further examine its ECSA and structural and compositional changes after the stability test in an acidic solution as an example. The subtle variations further confirm its high structural and chemical stability (fig. S22). The above observations confirm that these Ni-doped FeP/C hollow nanorods are highly active and stable HER electrocatalysts over the full pH range.

DISCUSSION

To validate the generality of this synthesis strategy for TMPs, Co-glycerate nanospheres, Ni-glycerate nanospheres, Cu-MOF ($[\text{Cu}_3(\text{btc})_2]_n$) polyhedrons, and ZIF-67 dodecahedrons are prepared as the templating precursors for synthesis of corresponding TMPs. TEM images show the similar morphology evolution process from solid precursors to hollow phosphides (fig. S23). XRD patterns (fig. S24) confirm the phase purity for each phosphide, including CoP (JCPDS card no. 29-0497), Ni_2P (JCPDS card no. 03-0953), and Cu_3P (JCPDS card no. 02-1263). Despite the dissimilarity in shape and composition, all these precursors can react with phytic acid and finally evolve into corresponding phosphides.

To provide deeper insight into the catalytic contribution from nickel doping at the atomic level, x-ray photoelectron spectroscopy (XPS) and spin-polarized density functional theory (DFT) calculations are performed. XPS analyses of the Fe 2p (Fig. 6, A and B) of FeP/C

and NFP/C-3 show two different chemical states with two additional satellite peaks. One is associated with FeP at lower binding energy and the other is Fe^{2+} or Fe^{3+} chemical environment at higher binding energy (40, 41). The ratio between the two iron chemical states ($\text{Fe}^{2+/3+}/\text{FeP}$) is 4.69 for FeP/C and 1.65 for NFP/C-3. For P 2p (Fig. 6, C and D), a pair of peaks at lower binding energy matches well with that of metal phosphide. A second pair of peaks at higher binding energy is assigned to a phosphate environment (40). The ratio between the two phosphorus chemical states (P-O/Fe-P) is 5.26 for FeP/C and 1.51 for NFP/C-3. Moreover, the weak signal of Ni 2p implies the presence of trace amount of nickel species (fig. S25). From the XPS analysis, it could be concluded that (i) the outermost surface of catalysts is oxidized to phosphates, (ii) the negative shift for Fe 2p and the positive shift for P 2p indicate the electron interactions with the transfer from P atoms to Fe atoms, and (iii) nickel doping can significantly increase the relative content of electrocatalytically active phosphides.

We find that the trends in binding strengths are generally preserved for coverages between the lowest hydrogen coverage rate (θ_{H}) and the coverage where HER occurs (junction point between solid lines and dotted lines in Fig. 6E) (42). For Pt, the best-known HER electrocatalyst, its hydrogen adsorption free energy (ΔG_{H^*}) changes little within a moderate range of -0.13 to 0.02 eV regardless of the alternation of θ_{H} . While for FeP, when the θ_{H} is below 50%, the ΔG_{H^*} is very low, implying strong bonding between adsorbed hydrogen and the catalyst. As a result, active sites are blocked to reduce HER efficiency. When the θ_{H} exceeds 50%, its ΔG_{H^*} becomes much lower again to suppress HER performance, which is consistent with the phenomenon reported by Jaramillo and co-workers (42). After nickel doping, the ΔG_{H^*} becomes higher, especially at a low θ_{H} of 25%, from -0.47 to -0.2 eV , implying the transfer of electrons from P atoms to Fe atoms, which is consistent

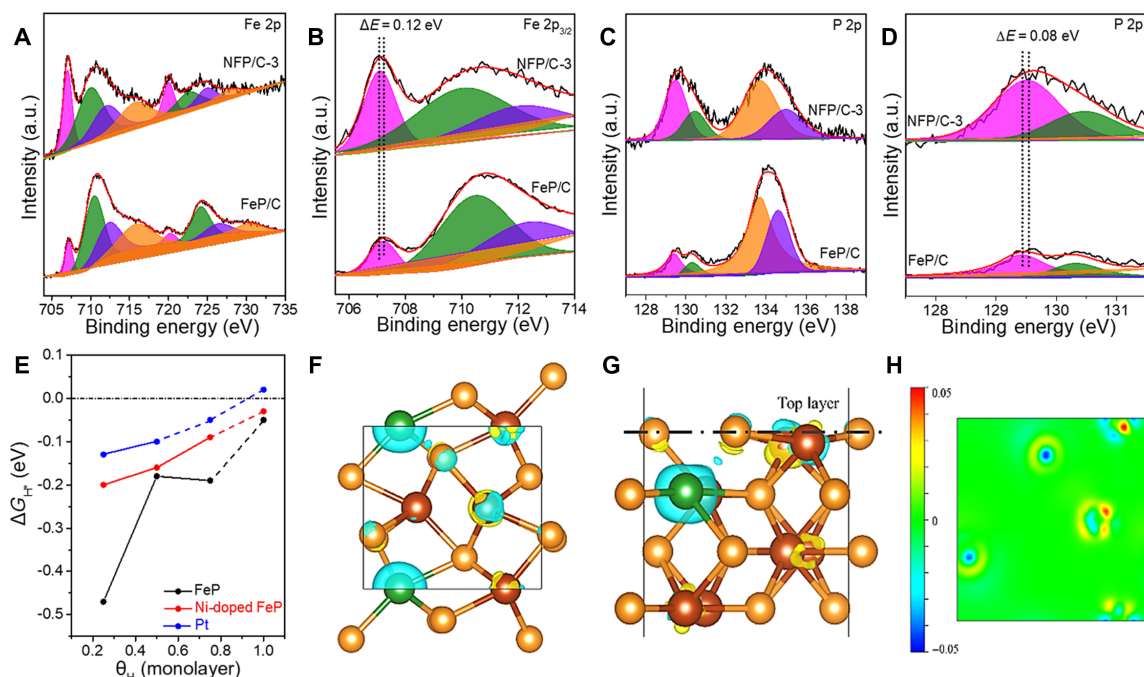


Fig. 6. XPS and DFT calculation results about the promotion of dopant on the catalytic performances. High-resolution XPS spectra of (A and B) Fe 2p and (C and D) P 2p for FeP/C and NFP/C-3; (E) ΔG_{H^*} as a function of θ_{H} for Pt, FeP, and Ni-doped FeP. (F to H) DFT-calculated electronic structures. (F) the charge density difference on Ni-doped FeP: $\rho = \rho[\text{Ni-FeP}] + \rho(\text{Fe}) - \rho[\text{Ni}] - \rho[\text{FeP}]$; yellow and cyan isosurfaces represent electron accumulation and electron depletion, respectively. (G) Section line and (H) isosurface two-dimensional view.

with the XPS results (Fig. 6, A to D). Besides, when the θ_{H} is up to 75%, the value of ΔG_{H^*} for Ni-doped FeP becomes closer to zero instead of lower for pure FeP, suggesting the more favorable HER process. This improvement of the kinetic process is also reflected by the decrease of the Tafel slope from 127 mV decade⁻¹ for FeP/C to 54 mV decade⁻¹ for NFP/C-3. The optimized structures for the above calculations can be seen in figs. S26 to S33. To further explore the principle of improving the material properties by nickel doping, the differential charge distribution calculation is performed. A large number of electron holes are generated around the Ni atom, indicating the occurrence of charge transfer (Fig. 6, F to H). The transfer of electrons from Ni atoms to P atoms increases the electron density around P atoms, resulting in weakened P–H bonding. Compared with pure FeP, the transfer of electrons leads to the lower binding energy of Fe 2p in Ni-doped FeP and stronger antioxidant capability. Meanwhile, the negative electrification of Fe atoms prevents the huge decrease of ΔG_{H^*} with the increase of θ_{H} . The weakened hydrogen adsorption and P–H bond both make H atoms more easily desorbed and more favorable for HER (43).

In summary, we present a facile route to synthesize Ni-doped FeP/C hollow nanorods with tunable aspect ratios based on the etching and coordination reaction between MOFs and phytic acid. Owing to the synergistic modulation of the component and the structural and electronic properties by the cationic dopant, the as-prepared hollow nanorods of Ni-doped FeP nanocrystals hybridized with carbon exhibit high electrocatalytic activities and superior stability for hydrogen evolution over the full pH range. The present strategy provides a general and effective route to design highly efficient pH-universal phosphide-based electrocatalysts with tunable chemical compositions and structures.

MATERIALS AND METHODS

Synthesis

Synthesis of MIL-88A hexagonal nanorods and Ni-doped MIL-88A hexagonal nanorods

According to the literature method (44), 1.2 mmol of fumaric acid was first dissolved in 25 ml of deionized (DI) water and stirred at 400 rpm at 70°C for 10 min. Then, 1.3 mmol of $\text{Fe}(\text{NO}_3)_3 \cdot 9\text{H}_2\text{O}$ was added into the solution and stirred for another 10 min. Last, the solution was transferred to a Teflon-lined stainless steel autoclave (40 ml in total capacity) and kept at 110°C for 6 hours. After cooling down to room temperature, the obtained MIL-88A hexagonal nanorods were separated by centrifugation, washed with DI water and ethanol, and finally dried in a vacuum drying oven. Ni-doped MIL-88A hexagonal nanorods were synthesized by the same method used for MIL-88A except that additional $\text{Ni}(\text{NO}_3)_2 \cdot 6\text{H}_2\text{O}$ was added into the solution. Ni-doped MIL-88A samples with different Ni contents are denoted as NM-1, NM-2, and NM-3 for Ni/Fe atomic ratios of 1:3, 2:2, and 3:1 in the reactants, respectively.

Synthesis of M-glycerate (M = Co, Ni) sphere precursors

According to our previously reported literature with slight modification (45), 0.108 g of cobalt nitrate hexahydrate and 8 ml of glycerol were dissolved into 40 ml of isopropanol, and after stirring for 40 min at 800 rpm, the as-prepared solution was then transferred to a Teflon-lined stainless steel autoclave and kept at 180°C for 6 hours. For Ni-glycerate, 0.145 g of nickel nitrate hexahydrate and 7.5 ml of glycerol were dissolved into 52.5 ml of isopropanol, and then 1 ml of water was dropped into the solution. After stirring for 40 min at 800 rpm, the as-

prepared solution was then transferred to a Teflon-lined stainless steel autoclave and kept at 200°C for 10 hours. The product was isolated using centrifugation, washed five times with ethanol, and dried at 80°C.

Synthesis of $[\text{Cu}_3(\text{btc})_2]_n$ polyhedron precursors

According to a previously reported literature with slight modification (46), 41.0 mg of copper nitrate trihydrate and 1.43 g of lauric acid were dissolved in 10 ml of butanol. The mixed solution was stirred at 400 rpm at 70°C until a transparent solution was obtained. Then, 20 mg of benzene-1,3,5-tricarboxylic acid was added and continuously stirred for another 10 min. The as-prepared solution was then transferred to a Teflon-lined stainless steel autoclave and kept at 140°C for 4 hours. The resulting blue powder was isolated using centrifugation, washed five times with ethanol, and dried at 80°C.

Synthesis of ZIF-67 polyhedron precursors

According to a previously reported literature with slight modification (47), a solution of cobalt acetate tetrahydrate (0.6 g in 5 ml of water) was added into a solution of 2-methylimidazole (2.24 g in 5 ml of water). The resulting mixture was aged at room temperature for 5 hours. Last, the purple precipitate was collected by centrifugation, washed three times with methanol, and dried for further use.

Synthesis of PTM and Ni-doped MIL-88A hollow samples

One hundred milligrams of as-prepared MIL-88A or Ni-doped MIL-88A was dispersed in 10 ml of DI water. After stirring for 10 min, 15 ml of phytic acid solution (0.1 M) was added into the above solutions; the solution was kept at 90°C for 3 hours. The acid-treated products were separated by centrifugation, washed with DI water and ethanol, and dried in a vacuum drying oven. The phytic acid-treated MIL-88A is denoted as PTM. The phytic acid-treated NM-1, NM-2, and NM-3 are denoted as PTNM-1, PTNM-2, and PTNM-3, respectively.

Synthesis of phytic acid-treated Co-glycerate, Ni-glycerate, Cu-MOF, and ZIF-67 precursors

One hundred milligrams of as-prepared Co-glycerate, Ni-glycerate, Cu-MOF, and ZIF-67 were dispersed in 15 ml of ethanol separately. After stirring for 10 min, 10 ml of phytic acid ethanol solution (0.1 M) was added into the above solutions and kept at room temperature for different durations (3 hours for Co-glycerate and Ni-glycerate and 30 min for Cu-MOF). Then, the acid-treated products were separated by centrifugation, washed with ethanol, and dried in a vacuum drying oven.

Synthesis of FeP/C and Ni-doped FeP/C hollow nanorods

The as-synthesized PTM and PTNM nanorods were transferred into a tube furnace and carbonized in a flowing H_2 (5%)/Ar atmosphere. Specifically, the materials were first heated from room temperature to 200°C with a ramp rate of 1°C min⁻¹ and kept for 2 hours. Then, the temperature was further increased to 800°C with the same rate and kept for another 2 hours.

Synthesis of hollow CoP nanospheres, core-shell Ni_2P nanospheres, shattered $\text{Cu}_3\text{P/C}$ nanoparticles, and hollow CoP/C polyhedrons

The as-synthesized phytic acid-treated Co-glycerate, Ni-glycerate, Cu-MOF, and ZIF-67 were transferred into a tube furnace and carbonized in a flowing H_2 (5%)/Ar atmosphere with the same calcination procedure and time for NFP/C-3.

Synthesis of NFP/C-3 with low crystallinity and without carbon

The NFP/C-3 with low crystallinity was prepared by the same method for NFP/C-3 except the annealing time, which was reduced from 2 hours to 0.5 and 1.0 hour. To prepare NFP-3 without carbon, PTNM-3

(100 mg) was calcined in air at 600°C for 3 hours with a ramp rate of 1°C min⁻¹ to consume carbon completely. Then, the obtained sample was immersed into 10 ml of phytic acid ethanol solution (0.1 M) and kept for 3 hours at room temperature. Afterward, phytic acid-treated oxides were annealed in a flowing H₂ (5%)/Ar atmosphere with the same annealing process for NFP/C-3.

Materials characterization

The morphology and structure of the products were characterized using FESEM (JEOL, JSM-6700F) and TEM (JEOL, JEM-1400). Elemental mapping images were collected using a TEM (JEOL, JEM-2100F) equipped with EDX spectroscopy. XRD patterns were collected on a Bruker D2 Phaser with Ni-filtered Cu K α radiation ($\lambda = 1.5406$ Å) at a voltage of 30 kV and a current of 10 mA. XPS (ESCALAB 250) was performed by an ESCALAB 250 x-ray photoelectron spectrometer to evaluate the chemical state of the elements on the surface of the materials. All XPS spectra were corrected using the C 1s line at 284.6 eV, and curve fitting and background subtraction were accomplished. Raman spectra were collected on a Renishaw Invia Reflex Raman microscope equipped with a 758-nm excitation laser. N₂ adsorption measurements were performed in an ASAP 2010 Micromeritics apparatus. The samples of MIL-88A, NM-1, NM-2, and NM-3 were evacuated at 423 K for 20 hours before analysis. The samples of FeP/C, NFP/C-1, NFP/C-2, and NFP/C-3 were evacuated at 473 K for 20 hours before analysis. The pore volume and pore size distribution were calculated from the N₂ adsorption curve by the Barrett-Joyner-Halenda (BJH) method. FTIR spectra were collected using a PerkinElmer FTIR spectrometer. Inductively coupled plasma atomic emission spectroscopy (ICP-AES) using a ThermoFisher iCAP6500Duo was used to analyze the concentration of nickel and iron.

Electrochemical measurements

All measurements were performed in a standard three-electrode system with a CHI 760E electrochemical workstation at room temperature. Hydrogen-saturated 0.5 M H₂SO₄, 1.0 M PBS, and 1.0 M KOH solutions were chosen as electrolytes for HER. A carbon rod and an Ag/AgCl electrode (KCl-saturated) were used as the counter electrode and the reference electrode, respectively, in all measurements except for the reference calibration. The preparation of the working electrodes containing the investigated catalysts can be found as follows. A suspension was prepared by dispersing catalysts (10 mg) in a solution of water and ethanol (2 ml, $V_{\text{water}}/V_{\text{ethanol}} = 1/4$), followed by the addition of 5 weight % Dupont Nafion 117 solution (50 μ l). The mixed solution was sonicated for 5 min to obtain a homogeneous catalyst ink. The dispersion (20 μ l) was pipetted onto a piece of clean CFP (0.5 cm by 0.5 cm), which was subjected to overnight solvent evaporation in air. The mass loading of catalysts was 0.4 mg cm⁻². Before the electrochemical measurements, the reference electrode was calibrated by performing cyclic voltammetry (CV) scans with a scan rate of 2.0 mV s⁻¹ in hydrogen-saturated electrolytes with a Pt wire, a Pt nanosheet, and an Ag/AgCl electrode as the counter electrode, the working electrode, and the reference electrode, respectively. The average of the two potentials where the current crossed zero was taken to be the thermodynamic potential for the hydrogen electrode reactions. All the LSV curves were carried out at 5.0 mV s⁻¹. The ohmic drop correction was performed by the method of positive feedback, and the compensation level is 95%. All LSV curves were corrected with *iR*-compensation. EIS measurements were conducted in the range of 0.01 to 10⁵ Hz with an amplitude of 0.01 V.

Computational methods

Spin-polarized DFT calculations were performed in the plane wave and ultrasoft pseudopotentials (USPP) as implemented in Quantum ESPRESSO. Adsorption energies were calculated using the Grimme-D² vdW-correction with Perdew-Burke-Ernzerhof exchange functional correction. The plane-wave cutoff and density cutoff were 25 and 225 Ry, respectively. FeP bulk lattice constants (relative error) were determined to be $a = 5.155$ Å (−0.73%), $b = 5.760$ Å (−0.55%), and $c = 3.054$ Å (−1.45%), in good agreement with experimentally measured values (48). All the atomic structures for the models were fully relaxed with self-consistency accuracy of 10⁻⁵ Ry, and the residual forces were within 10⁻³ Ry/bohr for geometry optimizations. The occupancy of the one-electron states was calculated using an electronic temperature of $\kappa_B T = 0.01$ Ry for surfaces and 0.001 Ry for molecules in vacuum. All energies were extrapolated to $T = 0$ K. A vacuum slab of 10 Å was used for surface isolation to prevent interaction between two surfaces (15 Å only change less than 1% energy), and the top atomic layers were relaxed with all other layers fixed to simulate bulk structure. Brillouin zone was simply using *k*-points with $5 \times 5 \times 1$ on slab (increase the Brillouin zone make little change to final energy) and $5 \times 5 \times 5$ on bulk structures.

Since θ_H is extremely important for the calculation of HER, especially for TMPs and sulfides, the exploration of θ_H is necessary (48). The θ_H is defined as the fraction of a monolayer with respect to the number of available sites on the basal plane

$$\theta_H = n_H / \text{Total sites}$$

$$\Delta G_{H^*} = \Delta E_H + \Delta E_{ZPE} - T\Delta S_H$$

where ΔE_H is the hydrogen chemisorption energy, ΔE_{ZPE} is the difference in zero-point energy between the adsorbed and the gas phase, and ΔS_H is the gas phase entropy change of H adsorption. ΔE_H is computed by $\Delta E_H = E_{\text{slab}+nH} - E_{\text{slab}} + (n-1)H - \frac{1}{2}E_{H_2}$, where n is the number of H atoms in the calculation. Moreover, $T\Delta S_H$ and ΔE_{ZPE} were obtained by following the scheme proposed by Nørskov *et al.* (49): The entropy of adsorption of 0.5H₂ is $\Delta S_H \approx -1/2S_{H_2}^0$, where $S_{H_2}^0$ is the entropy of H₂ in the gas phase at standard conditions. The (002) plane observed by HRTEM was selected for calculation, and no other planes were discussed in this paper.

SUPPLEMENTARY MATERIALS

Supplementary material for this article is available at <http://advances.sciencemag.org/cgi/content/full/5/2/eaav6009/DC1>

Fig. S1. Histograms for the rod length and width distribution of MIL-88A with different doping amounts.

Fig. S2. The influence of dopant amount on the pore size distribution of MIL-88A.

Fig. S3. The influence of temperature of phytic acid solution on the morphology and structure of NM-3 nanorods.

Fig. S4. The influence of temperature of phytic acid solution on the composition of NM-3 nanorods.

Fig. S5. Morphology and structure characterizations of FeP/C, NFP/C-1, and NFP/C-2.

Fig. S6. Elemental composition characterizations of NFP/C-3 hollow nanorods.

Fig. S7. Characterization of the carbon in the hybrids.

Fig. S8. The nitrogen sorption characterizations of as-prepared phosphides.

Fig. S9. Reference electrode calibrations.

Fig. S10. Calculations of the onset potential in 0.5 M H₂SO₄ solution.

Fig. S11. The contribution of the CFP substrate toward HER.

Fig. S12. The influences of temperature and time on composition and crystallinity.

Fig. S13. The influence of crystallinity on electrochemical performances.

Fig. S14. Structure and composition characterizations of Ni-doped Fe₂O₃ and Ni-doped FeP.

Fig. S15. The influence of carbon on electrochemical performances.

Fig. S16. Calculations of the exchange current density in 0.5 M H₂SO₄ solution.

Fig. S17. CV curves at different scan rates in 0.5 M H₂SO₄ solution.
 Fig. S18. Characterizations of R_s and R_{ct} in 0.5 M H₂SO₄ solution.
 Fig. S19. Characterization of hydrophilicity.
 Fig. S20. Calculations of the onset potential and exchange current density for NFP/C-3 in 1.0 M KOH and 1.0 M PBS solutions.
 Fig. S21. Stability performances of NFP/C-3 in 0.5 M H₂SO₄, 1.0 M PBS, and 1.0 M KOH solutions.
 Fig. S22. Electrochemistry, structure, and composition characterizations of NFP/C-3 after HER stability test in 0.5 M H₂SO₄ solution.
 Fig. S23. Morphological characterization of as-prepared metal phosphides with various shapes derived from different precursors.
 Fig. S24. XRD patterns of as-prepared metal phosphides.
 Fig. S25. High-resolution XPS spectra of C 1s and Ni 2p.
 Fig. S26. The optimized unit cell vc-relaxation of FeP.
 Fig. S27. Optimized structures of FeP (002) with different sites.
 Fig. S28. Optimized structures of FeP (002) with different sites at a θ_H of 50%.
 Fig. S29. Optimized structures of FeP (002) with different sites at a θ_H of 75% and 100%.
 Fig. S30. Optimized structures of Ni-doped FeP.
 Fig. S31. Optimized structures of Ni-doped FeP with different sites.
 Fig. S32. Optimized structures of Ni-doped FeP with different sites at a θ_H of 50%.
 Fig. S33. Optimized structures of Ni-doped FeP with different sites at a θ_H of 75 and 100%.
 Table S1. Comparisons of the electrocatalytic activities of FeP/C and Ni-doped FeP/C in 0.5 M H₂SO₄ solution.
 Table S2. Comparison of the electrocatalytic activities of NFP/C-3 with some representative HER electrocatalysts in 0.5 M H₂SO₄ solution.
 Table S3. Comparison of the electrocatalytic activities of NFP/C-3 with some representative phosphide-based HER electrocatalysts recently reported in neutral/alkaline media.
 Table S4. Calculation details about atomic positions for FeP (002).
 Table S5. Calculation details about atomic positions for Ni-doped FeP (002).

REFERENCES AND NOTES

- J. A. Turner, Sustainable hydrogen production. *Science* **305**, 972–974 (2004).
- P. P. Edwards, V. L. Kuznetsov, W. I. F. David, N. P. Brandon, Hydrogen and fuel cells: Towards a sustainable energy future. *Energy Policy* **36**, 4356–4362 (2008).
- H. Jin, C. Guo, X. Liu, J. Liu, A. Vasileff, Y. Jiao, Y. Zheng, S. Z. Qiao, Emerging two-dimensional nanomaterials for electrocatalysis. *Chem. Rev.* **118**, 6337–6408 (2018).
- Y. Zheng, Y. Jiao, A. Vasileff, S. Z. Qiao, The hydrogen evolution reaction in alkaline solution: From theory, single crystal models, to practical electrocatalysts. *Angew. Chem. Int. Ed.* **57**, 7568–7579 (2018).
- Y. Pi, Q. Shao, P. Wang, J. Guo, X. Huang, General formation of monodisperse IrM (M = Ni, Co, Fe) bimetallic nanoclusters as bifunctional electrocatalysts for acidic overall water splitting. *Adv. Funct. Mater.* **27**, 1700886 (2017).
- J. Liu, D. Zhu, T. Ling, A. Vasileff, S. Z. Qiao, S-NiFe₂O₄ ultra-small nanoparticle built nanosheets for efficient water splitting in alkaline and neutral pH. *Nano Energy* **40**, 264–273 (2017).
- T. Ling, D.-Y. Yan, H. Wang, Y. Jiao, Z. Hu, Y. Zheng, L. Zheng, J. Mao, H. Liu, X.-W. Du, M. Jaroniec, S. Z. Qiao, Activating cobalt (II) oxide nanorods for efficient electrocatalysis by strain engineering. *Nat. Commun.* **8**, 1509 (2017).
- H. B. Wu, B. Y. Xia, L. Yu, X.-Y. Yu, X. W. Lou, Porous molybdenum carbide nano-octahedrons synthesized via confined carburization in metal-organic frameworks for efficient hydrogen production. *Nat. Commun.* **6**, 6512 (2015).
- C. Bae, T. A. Ho, H. Kim, S. Lee, S. Lim, M. Kim, H. Yoo, J. M. Montero-Moreno, J. H. Park, H. Shin, Bulk layered heterojunction as an efficient electrocatalyst for hydrogen evolution. *Sci. Adv.* **3**, e1602215 (2017).
- W.-F. Chen, K. Sasaki, C. Ma, A. I. Frenkel, N. Marinkovic, J. T. Muckerman, Y. Zhu, R. R. Adzic, Hydrogen-evolution catalysts based on non-noble metal nickel-molybdenum nitride nanosheets. *Angew. Chem. Int. Ed.* **51**, 6131–6135 (2012).
- H. Li, S. Chen, H. Lin, X. Xu, H. Yang, L. Song, X. Wang, Nickel diselenide ultrathin nanowires decorated with amorphous nickel oxide nanoparticles for enhanced water splitting electrocatalysis. *Small* **13**, 1701487 (2017).
- Z. Peng, S. Yang, D. Jia, P. Da, P. He, A. M. Al-Enizi, G. Ding, X. Xie, G. Zheng, Homologous metal-free electrocatalysts grown on three-dimensional carbon networks for overall water splitting in acidic and alkaline media. *J. Mater. Chem. A* **4**, 12878–12883 (2016).
- T. Liu, X. Ma, D. Liu, S. Hao, G. Du, Y. Ma, A. M. Asiri, X. Sun, L. Chen, Mn doping of CoP nanosheets array: An efficient electrocatalyst for hydrogen evolution reaction with enhanced activity at all pH values. *ACS Catal.* **7**, 98–102 (2017).
- Z. H. Pu, I. S. Amiinu, C. Zhang, M. Wang, Z. Kou, S. Mu, Phytic acid-derivative transition metal phosphides encapsulated in N-P-codoped carbon: An efficient and durable hydrogen evolution electrocatalyst in a wide pH range. *Nanoscale* **9**, 3555–3560 (2017).
- R. Zhang, X. Wang, S. Yu, T. Wen, X. Zhu, F. Yang, X. Sun, X. Wang, W. Hu, Ternary NiCo₂P_x nanowires as pH-universal electrocatalysts for highly efficient hydrogen evolution reaction. *Adv. Mater.* **29**, 1605502 (2017).
- Z. Xing, Q. Liu, A. M. Asiri, X. Sun, High-efficiency electrochemical hydrogen evolution catalyzed by tungsten phosphide submicroparticles. *ACS Catal.* **5**, 145–149 (2015).
- S. T. Oyama, Novel catalysts for advanced hydroprocessing: Transition metal phosphides. *J. Catal.* **216**, 343–352 (2003).
- D. Y. Chung, S. W. Jun, G. Yoon, H. Kim, J. M. Yoo, K.-S. Lee, T. Kim, H. Shin, A. K. Sinha, S. G. Kwon, K. Kang, T. Hyeon, Y.-E. Sung, Large-scale synthesis of carbon-shell-coated FeP nanoparticles for robust hydrogen evolution reaction electrocatalyst. *J. Am. Chem. Soc.* **139**, 6669–6674 (2017).
- Y. Xu, R. Wu, J. Zhang, Y. Shi, B. Zhang, Anion-exchange synthesis of nanoporous FeP nanosheets as electrocatalysts for hydrogen evolution reaction. *Chem. Commun.* **49**, 6656–6658 (2013).
- X. Zhu, M. Liu, Y. Liu, R. Chen, Z. Nie, J. Li, S. Yao, Carbon-coated hollow mesoporous FeP microcubes: An efficient and stable electrocatalyst for hydrogen evolution. *J. Mater. Chem. A* **4**, 8974–8977 (2016).
- P. Jiang, Q. Liu, Y. Yang, J. Tian, A. Asiri, X. Sun, A cost-effective 3D hydrogen evolution cathode with high catalytic activity: FeP nanowire array as the active phase. *Angew. Chem. Int. Ed.* **53**, 12855–12859 (2014).
- Y. Liang, Q. Liu, A. M. Asiri, X. Sun, Y. Luo, Self-supported FeP nanorod arrays: A cost-effective 3D hydrogen evolution cathode with high catalytic activity. *ACS Catal.* **4**, 4065–4069 (2014).
- C. Y. Son, I. H. Kwak, Y. R. Lim, J. Park, FeP and FeP₂ nanowires for efficient electrocatalytic hydrogen evolution reaction. *Chem. Commun.* **52**, 2819–2822 (2016).
- L. Yu, H. Hu, H. B. Wu, X. W. Lou, Complex hollow nanostructures: Synthesis and energy-related applications. *Adv. Mater.* **29**, 1604563 (2017).
- E. J. Popczun, J. R. McKone, C. G. Read, A. J. Biacchi, A. M. Wiltrout, N. S. Lewis, R. E. Schaak, Nanostructured nickel phosphide as an electrocatalyst for the hydrogen evolution reaction. *J. Am. Chem. Soc.* **135**, 9267–9270 (2013).
- H. B. Wu, X. W. Lou, Metal-organic frameworks and their derived materials for electrochemical energy storage and conversion: Promises and challenges. *Sci. Adv.* **3**, eaap9252 (2017).
- H. Tabassum, W. Guo, W. Meng, A. Mahmood, R. Zhao, Q. Wang, R. Zou, Metal-organic frameworks derived cobalt phosphide architecture encapsulated into B/N co-doped graphene nanotubes for all pH value electrochemical hydrogen evolution. *Adv. Energy Mater.* **7**, 1601671 (2017).
- J. Tang, Y. Yamauchi, Carbon materials: MOF morphologies in control. *Nat. Chem.* **8**, 638–639 (2016).
- C. Young, J. Wang, J. Kim, Y. Sugahara, J. Henzie, Y. Yamauchi, Controlled chemical vapor deposition for synthesis of nanowire arrays of metal-organic frameworks and their thermal conversion to carbon/metal oxide hybrid materials. *Chem. Mater.* **30**, 3379–3386 (2018).
- W. Zhang, X. Jiang, Y. Zhao, A. Carné-sánchez, V. Malgras, J. Kim, J. H. Kim, S. Wang, J. Liu, J.-S. Jiang, Y. Yamauchi, M. Hu, Hollow carbon nanobubbles: Monocrystalline MOF nanobubbles and their pyrolysis. *Chem. Sci.* **8**, 3538–3546 (2017).
- R. R. Salunkhe, C. Young, J. Tang, T. Takei, Y. Ide, N. Kobayashi, Y. Yamauchi, A high-performance supercapacitor cell based on ZIF-8-derived nanoporous carbon using an organic electrolyte. *Chem. Commun.* **52**, 4764–4767 (2016).
- C. Tang, R. Zhang, W. Lu, L. He, X. Jiang, A. M. Asiri, X. Sun, Fe-doped CoP nanoarray: A monolithic multifunctional catalyst for highly efficient hydrogen generation. *Adv. Mater.* **29**, 1602441 (2017).
- T. Chalati, P. Horcajada, R. Gref, P. Couvreur, C. Serre, Optimisation of the synthesis of MOF nanoparticles made of flexible porous iron fumarate MIL-88A. *J. Mater. Chem.* **21**, 2220–2227 (2011).
- L. Wang, Y. Zhang, X. Li, Y. Xie, J. He, J. Yu, Y. H. Song, The MIL-88A-derived Fe₃O₄-carbon hierarchical nanocomposites for electrochemical sensing. *Sci. Rep.* **5**, 14341 (2015).
- J. Zhang, L. Qu, G. Shi, J. Liu, J. Chen, L. Dai, N. P-codoped carbon networks as efficient metal-free bifunctional catalysts for oxygen reduction and hydrogen evolution reactions. *Angew. Chem. Int. Ed.* **55**, 2230–2234 (2016).
- J.-S. Li, X.-R. Wang, J.-Y. Li, S. Zhang, J.-Q. Sha, G.-D. Liu, B. Tang, Pomegranate-like molybdenum phosphide@phosphorus-doped carbon nanospheres coupled with carbon nanotubes for efficient hydrogen evolution reaction. *Carbon* **139**, 234–240 (2018).
- J. Tian, Q. Liu, N. Cheng, A. M. Asiri, X. Sun, Self-supported Cu₃P nanowire arrays as an integrated high-performance three-dimensional cathode for generating hydrogen from water. *Angew. Chem. Int. Ed.* **53**, 9577–9581 (2014).
- H. Li, S. Lu, J. Sun, J. Pei, D. Liu, Y. Xue, J. Mao, W. Zhu, Z. Zhuang, Phase controlled synthesis of nickel phosphide nanocrystals and their electrocatalytic performance for hydrogen evolution reaction. *Chem. -Eur. J.* **24**, 11748–11754 (2018).

39. X. Wang, Y. V. Kolen'Ko, X.-Q. Bao, K. Kovnir, L. Liu, One-step synthesis of self-supported nickel phosphide nanosheet array cathodes for efficient electrocatalytic hydrogen generation. *Angew. Chem. Int. Ed.* **54**, 8188–8192 (2015).
40. K. Liu, C. Zhang, Y. Sun, G. Zhang, X. Shen, F. Zhou, H. Zhang, Z. Wu, E. C. Wegener, C. J. Taubert, J. T. Miller, Z. Peng, Y. Zhu, High-performance transition metal phosphide alloy catalyst for oxygen evolution reaction. *ACS Nano* **12**, 158–167 (2018).
41. Z. Zhang, B. Lu, J. Hao, W. Yang, J. Tang, FeP nanoparticles grown on graphene sheets as highly active non-precious-metal electrocatalysts for hydrogen evolution reaction. *Chem. Commun.* **50**, 11554–11557 (2014).
42. J. Kibsgaard, C. Tsai, K. Chan, J. D. Benck, J. K. Nørskov, F. Abild-Pedersen, T. F. Jaramillo, Designing an improved transition metal phosphide catalyst for hydrogen evolution using experimental and theoretical trends. *Energy Environ. Sci.* **8**, 3022–3029 (2015).
43. Y. Ito, W. Cong, T. Fujita, Z. Tang, M. Chen, High catalytic activity of nitrogen and sulfur co-doped nanoporous graphene in the hydrogen evolution reaction. *Angew. Chem. Int. Ed.* **54**, 2131–2136 (2015).
44. P. Horcajada, T. Chalati, C. Serre, B. Gillet, C. Sebrie, T. Baati, J. F. Eubank, D. Heurtaux, P. Clayette, C. Kreuz, J.-S. Chang, Y. K. Hwang, V. Marsaud, P.-N. Bories, L. Cynober, S. Gil, G. Férey, P. Couvreur, R. Gref, Porous metal–organic-framework nanoscale carriers as a potential platform for drug delivery and imaging. *Nat. Mater.* **9**, 172–178 (2010).
45. L. Shen, L. Yu, X.-Y. Yu, X. Zhang, X. W. Lou, Self-templated formation of uniform NiCo₂O₄ hollow spheres with complex interior structures for lithium-ion batteries and supercapacitors. *Angew. Chem. Int. Ed.* **54**, 1868–1872 (2015).
46. A. Umemura, S. Diring, S. Furukawa, H. Uehara, T. Tsuruoka, S. Kitagawa, Morphology design of porous coordination polymer crystals by coordination modulation. *J. Am. Chem. Soc.* **133**, 15506–15513 (2011).
47. C. Avci, J. Ariñez-Soriano, A. Carné-Sánchez, V. Guillerme, C. Carbonell, I. Imaz, D. Maspoch, Post-synthetic anisotropic wet-chemical etching of colloidal sodalite ZIF crystals. *Angew. Chem. Int. Ed.* **54**, 14417–14421 (2015).
48. E. P. Elsukov, Y. N. Vorobev, A. V. Trubachev, V. A. Barinov, Structure and magnetic properties of Fe-P electrodeposited alloys. *Phys. Status Solidi A* **117**, 291–298 (1990).
49. J. K. Nørskov, T. Bligaard, A. Logadottir, J. R. Kitchin, J. G. Chen, S. Pandalov, U. Stimming, Trends in the exchange current for hydrogen evolution. *J. Electrochem. Soc.* **152**, J23–J26 (2005).

Acknowledgments

Funding: X.W.L. is grateful to the National Research Foundation (NRF) of Singapore for financial support through the NRF Investigatorship (NRF-NRFI2016-04). **Author contributions:** X.F.L. and X.W.L. conceived the idea and co-wrote the manuscript. X.F.L. carried out the materials synthesis and electrochemical evaluation. L.Y. helped with the materials characterizations. All the authors discussed the results and commented on the manuscript. **Competing interests:** The authors declare that they have no competing interests. **Data and materials availability:** All data needed to evaluate the conclusions in the paper are present in the paper and/or the Supplementary Materials. Additional data related to this paper may be requested from the authors.

Submitted 2 October 2018

Accepted 4 January 2019

Published 15 February 2019

10.1126/sciadv.aav6009

Citation: X. F. Lu, L. Yu, X. W. Lou, Highly crystalline Ni-doped FeP/carbon hollow nanorods as all-pH efficient and durable hydrogen evolving electrocatalysts. *Sci. Adv.* **5**, eaav6009 (2019).

Highly crystalline Ni-doped FeP/carbon hollow nanorods as all-pH efficient and durable hydrogen evolving electrocatalysts

Xue Feng Lu, Le Yu and Xiong Wen (David) Lou

Sci Adv **5** (2), eaav6009.
DOI: 10.1126/sciadv.aav6009

ARTICLE TOOLS

<http://advances.sciencemag.org/content/5/2/eaav6009>

SUPPLEMENTARY MATERIALS

<http://advances.sciencemag.org/content/suppl/2019/02/11/5.2.eaav6009.DC1>

REFERENCES

This article cites 49 articles, 4 of which you can access for free
<http://advances.sciencemag.org/content/5/2/eaav6009#BIBL>

PERMISSIONS

<http://www.sciencemag.org/help/reprints-and-permissions>

Use of this article is subject to the [Terms of Service](#)

Science Advances (ISSN 2375-2548) is published by the American Association for the Advancement of Science, 1200 New York Avenue NW, Washington, DC 20005. 2017 © The Authors, some rights reserved; exclusive licensee American Association for the Advancement of Science. No claim to original U.S. Government Works. The title *Science Advances* is a registered trademark of AAAS.